



**HAL**  
open science

# Narrow electromagnetic beam propagation in a graphene-like triangular metallic photonic structure

Kang Wang

► **To cite this version:**

Kang Wang. Narrow electromagnetic beam propagation in a graphene-like triangular metallic photonic structure. 2021. hal-03087584v2

**HAL Id: hal-03087584**

**<https://hal.science/hal-03087584v2>**

Preprint submitted on 4 Jan 2021 (v2), last revised 28 Jul 2021 (v3)

**HAL** is a multi-disciplinary open access archive for the deposit and dissemination of scientific research documents, whether they are published or not. The documents may come from teaching and research institutions in France or abroad, or from public or private research centers.

L'archive ouverte pluridisciplinaire **HAL**, est destinée au dépôt et à la diffusion de documents scientifiques de niveau recherche, publiés ou non, émanant des établissements d'enseignement et de recherche français ou étrangers, des laboratoires publics ou privés.

# Narrow electromagnetic beam propagation in a graphene-like triangular metallic photonic structure

Kang Wang\*

*Laboratoire de Physique des Solides, CNRS, Université Paris-Saclay, 91405 Orsay, France*

We study the propagation of narrow electromagnetic beams associated to different K-valleys, from both the armchair and zigzag edges, in a graphene-like triangular metallic photonic structure. Due to the metallic nature of the structure, the propagation of an electromagnetic wave, with wave vector close to the quasi-triangular iso-frequency contours of the Dirac cones resulting from the band trigonal warping, can be considered as being based on series of bonding or anti-bonding states, formed by the local resonance modes in the unit cells. The transmission of a narrow incident beam depends on the local structure configurations in the beam impact zone, that determine the distribution of the excited local resonance modes as well as the coupling between the latter and the incident field, thus the beam propagation in different directions. This investigation allows us to understand the interaction between an incident field and the resonance states associated to the Dirac cones at elementary structure scales reaching the size of these states. It can find application in valley photonics for transport tuning and optimization.

## I. INTRODUCTION

Graphene-like photonic structures are widely studied both for their fundamental interest and application potential. Indeed, these structures reproduce the electronic bands in atomic structures by creating Dirac cones in their frequency bands [1]. An electromagnetic (EM) emission can be coupled to such structures and the resulting spectrum modifications provide information on the dispersion properties of the Dirac cones as well as on the coupling with the incident field. Being geometrically and materially tunable, such photonic structures enable investigations of the physical properties inaccessible in atomic structures, by allowing structure configurations and modulations unrealizable in the latter. Many fundamental phenomena specific to the Dirac cones, including conical diffraction, gap soliton, pseudo-diffusive transmission, quantum Hall-like effect, zero refractive index and valley-polarized beam propagation [1–5], have been investigated. Potential applications, such as valley photonics exploring optically the valley degree of freedom to control and manipulate the light beam propagation, analogous to valleytronics [6], have recently been proposed for information processing [7]. Indeed, it is shown that, by lifting the inversion symmetry in the structures, it is possible to achieve photonic topological insulators for large-scale photonic integrations [8], and independent control of valley-dependent transportation [9].

Dirac cones can emerge in various dielectric [1–4, 10] and metallic [11–13] photonic structures. In the former, the band formation can be described by a nearly-free-photon approximation [14], while, in the latter, the low-frequency EM bands are formed by cavity-like local resonance modes confined inside the structure tiles delimited by metallic elements [12, 13, 15]. Such resonance modes follow a honeycomb distribution in a triangular metallic

structure, that is equivalent to a honeycomb atomic one.

It is a known fact that, due to the local 3-fold symmetry in a honeycomb structure, the Dirac cones undergo trigonal warping for frequencies departing from the Dirac level [16], that lifts the degeneracy between two inequivalent cones. The group velocity distribution becomes increasingly anisotropic. When the iso-frequency contours of the Dirac cones become nearly triangular, the wave propagation will follow the  $\Gamma$ -K directions that are perpendicular to the iso-frequency contours, and a beam propagating in such a structure undergoes splitting and self-collimation associated to different K valleys [5]. This provides an alternative way for wave propagation control and beam manipulation. Studies on K-valley dependent EM beam propagation, associated to the lower Dirac cones in dielectric photonic structures [5, 17] and to the upper cones in analogous situations of electron beams in atomic graphenes [18, 20], are both carried out. Beam splitting and self-collimation are obtained for the zigzag and armchair incidences.

Due to the huge value of the dielectric function of the metallic elements, metallic photonic structures need only a few number of periods to achieve band gaps [21], allowing smaller sample sizes in practice. And, more particularly, in a metallic structure, the eigenmodes of the low frequency crystal wave function can be constructed by the combination of the local resonance modes mentioned above in a tight binding (TB) model [12, 13, 15]. An EM wave propagating in a metallic structure will then follow the structural tile distribution, through the coupling between the local resonance modes. We have shown previously that an EM beam propagation associated to trigonally warped Dirac cones in a graphene-like triangular metallic photonic structure display drastically different behaviors as compared to the dielectric and other analogous systems, due to the EM wave function symmetry along the  $\Gamma$ -K lines and the metallic nature of the structure. Namely, at the armchair edge, the incident beam associated to the lower Dirac cone is collimated to one

---

\* kang.wang@universite-paris-saclay.fr

central beam, and that associated to the upper cone is split to two beams with a  $2\pi/3$  angle. The other expected beams are all strongly inhibited [19].

In this work we report a study of the transmission of narrow incident beams, of widths of the crystal period scales, from both the armchair and zigzag edges in a triangular metallic photonic structure, associated to the trigonally warped Dirac cones. We discuss the EM frequency band structure close to the quasi-triangular iso-frequency contours of a Dirac cones, and show that the beam transmission depends on the position and orientation of unit cells along the propagation directions in the beam impact zone, that will determine the characteristics of the excited local resonance modes and the coupling between the latter and the incident field, thus the beam propagation in different directions.

## II. BAND STRUCTURE CLOSE TO QUASI-TRIANGULAR ISO-FREQUENCY CONTOURS OF A DIRAC CONE

A triangular lattice [Fig. 1(a)] belongs to the symmetry group  $D_{6h}$  and contains two families of triangular tiles A and B, pointing respectively up- and downward in the figure. The metallic structure is constructed by infinite cylinders, with radius  $r = 0.25a$  ( $a$  being the lattice constant) and dielectric constant set to negative infinity, placed at the lattice nodes in an air background. The EM frequency band diagram for TM polarization (the electric field parallel to  $z$  axis), obtained by solving Maxwell's equations using the Finite-difference time-domain (FDTD) method, is reproduced in Fig. 1(b). Dirac cones are formed by the first two bands [12, 19]. The lower and upper Dirac cones at K point, depicted by iso-frequency contours, are reproduced in the same figure [(c) and (d)]. As a matter of fact, departing from the Dirac frequency  $\omega_D \approx 0.917$  ( $\omega a/2\pi c$ ), the iso-frequency lines undergo trigonal distortion and approach quasi-triangular forms at  $\omega_1 \approx 0.863$  and  $\omega_2 \approx 0.978$  ( $\omega a/2\pi c$ ) for respectively the lower and the upper cones.

The formation of the first two bands can be described by a TB model [12] [solid lines in Fig. 1(b)]. Recalling that, in a such model, the crystal wave function is expressed as the sum of local wave functions,  $|\phi_A\rangle$  and  $|\phi_B\rangle$ , corresponding to the electric field distributions of the  $s$ -like resonance modes formed inside A and B tiles delimited by three metallic cylinders at the vertices. Along  $\Gamma$ -K direction, the modes  $|\phi_A\rangle$  and  $|\phi_B\rangle$  contribute equally, in absolute value, to the crystal wave function:

$$|\Psi_{\mathbf{k}}(\mathbf{r})\rangle = \sum_m \frac{e^{i\mathbf{k}\cdot\mathbf{R}_m}}{\sqrt{2N}} (|\phi_A(\mathbf{r} - \mathbf{R}_m - \mathbf{d}_A)\rangle \pm |\phi_B(\mathbf{r} - \mathbf{R}_m - \mathbf{d}_B)\rangle) \quad (1)$$

with  $\sum_m$  summing over the unit cells. The wave function is characterized by a mirror or a mirror inversion symmetry

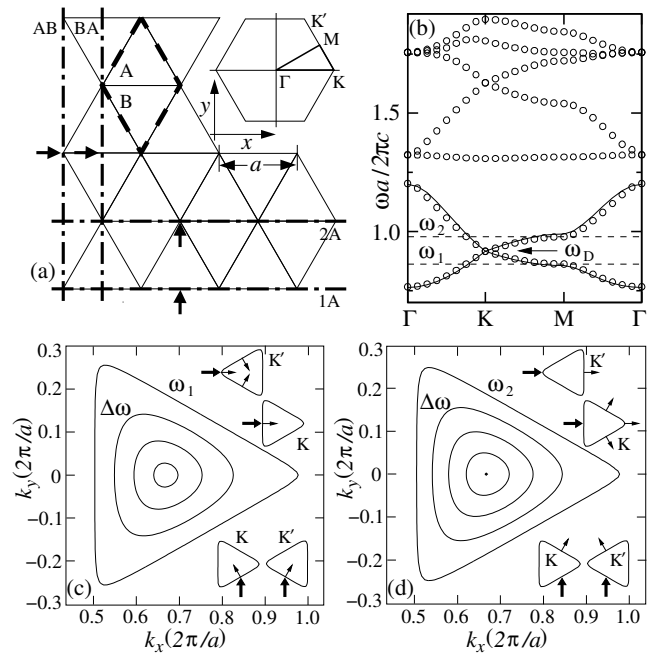


FIG. 1. The triangular lattice and its rhombic unit cell (thick dashed lines) [(a)] of the metallic photonic structure and the corresponding EM frequency band diagram [(b)], where a Dirac point at K ( $4\pi/3a, 0$ ) is obtained for  $\omega_D \approx 0.917$ . Iso-frequency contours of the lower and upper cone at the same K point, with contour interval  $\Delta\omega = 0.015$ , are depicted in (c) and (d). Quasi-triangular forms are obtained at frequency levels  $\omega_1 \approx 0.863$  and  $\omega_2 \approx 0.978$ , indicated by the dashed lines in (b) (All the values are normalized to  $\omega a/2\pi c$ ). The upper and lower insets in (c) and (d) depict the expected beam propagation directions (thin arrows) for respectively the armchair and zigzag edge incidence (thick arrows). The incidence edges investigated in the present work are depicted by the dash-dotted lines in (a).

with respect to the plane defined by the  $\Gamma$ -K line and the  $z$  axis.

Defining the usual parameters,  $\alpha$ ,  $\gamma$  and  $\beta$ , that describe, respectively, the overlap and the energy transfer between first neighbor tiles and the mode energy level shift from that in an individual tile [22], the crystal frequency  $\omega_k$  is the root of the characteristic equation [12]

$$\det \begin{bmatrix} \omega_0^2 - \beta - \omega_k^2 & -\xi[\gamma - \alpha(\omega_0^2 - \omega_k^2)] \\ -\xi^*[\gamma - \alpha(\omega_0^2 - \omega_k^2)] & \omega_0^2 - \beta - \omega_k^2 \end{bmatrix} = 0 \quad (2)$$

with  $\omega_0$  the eigenfrequency of the  $s$ -like resonance modes in an individual triangular tile, and, considering the  $x$  axis that is one of the  $\Gamma$ -K lines for simplicity,

$$\xi = 1 + 2\cos(k_x a/2) \quad (3)$$

The roots are simply

$$\omega_k^2 = \omega_0^2 - \frac{\beta \mp |\xi|\gamma}{1 \mp |\xi|\alpha} \quad (4)$$

The value of  $\omega_0$  can be obtained by solving Maxwell's equation using the FDTD method on an individual triangular tile.

Always along the  $x$  axis, as can be seen in Fig. 1(c) and (d), the left edges of the quasi-triangular contours are close to the wave vector  $k = (\pi/a, 0)$ . Indeed, one can check that the vector magnitude differences between the former and the latter are less than 1%. Therefore, wave vectors close to the edges of quasi-triangular contours are close to  $k = (\pi/a, 0)$  as well. For such wave vectors,  $\cos(k_x a/2)$  tends to zero, and Eq. (4) can be rewritten as

$$\omega_k^2 \approx \Omega_0^2 - \frac{\mp 2 \cos(k_x a/2) \gamma}{1 \mp \alpha} \quad (5)$$

with

$$\Omega^2 = \omega_0^2 - \frac{\beta \mp \gamma}{1 \mp \alpha} \quad (6)$$

( $\mp$  corresponding to the upper and lower Dirac cone, respectively.)

The above relation between the wave vectors can also be checked by considering the corresponding frequency levels. Indeed, the values of  $\Omega$  are exactly the crystal frequency levels at  $k = (\pi/a, 0)$ , where  $\xi$  is unity [Eqs. (3), (4) and (6)]. We get from the FDTD solutions  $\omega_{(\pi/a, 0)_1} = \Omega_1 \approx 0.8626$  and  $\omega_{(\pi/a, 0)_2} = \Omega_2 \approx 0.9792$  ( $\omega a/2\pi c$ ). These values are close to the frequency levels of the quasi-triangular contours  $\omega_1$  and  $\omega_2$  given above.

As a matter of fact, the  $\Omega^2$  expression in Eq. (6) corresponds to the energy levels of two coupled modes  $|\phi_A\rangle$  and  $|\phi_B\rangle$  in a unit cell, of which the long diagonal is perpendicular to the  $x$  axis, with  $\mp$  corresponding respectively to the anti-bonding and bonding states. The band structure along a  $\Gamma$ -K direction close to the quasi-triangular contours, associated to the lower or upper parts of the Dirac cones, can then be viewed as arising from series of  $|\phi_A\rangle$ - $|\phi_B\rangle$  bonding or anti-bonding states on one dimensional chains, with the band frequency derived from the  $\Omega$  values adjusted by a supplementary term, that takes the simple form in Eq. (5) along the  $x$  axis.

Along the  $\Gamma$ -K direction, the  $D_{6h}$  symmetry is lowered to that of a subgroup  $C_{2v}$  [23]. The  $|\phi_A\rangle$ - $|\phi_B\rangle$  bonding and anti-bonding states, as well as the crystal wave function, can be described by the  $A_1$  and  $B_1$  representations of  $C_{2v}$ , characterized by respectively a mirror and a mirror inversion symmetry with respect to the  $\Gamma$ -K- $z$  plane. An EM beam propagating along the  $\Gamma$ -K direction and associated to the lower Dirac cone is described by the  $A_1$  representation, while a such beam associated to the upper cone by  $B_1$  [19]. They will be referred to as  $A_1$  and  $B_1$  beams hereinafter.

In the present triangular structure, a  $|\phi_A\rangle$ - $|\phi_B\rangle$  bonding or anti-bonding state can only be formed in a rhombic unit cell, since the coupling takes place through the opening at the common edge between A and B tiles [see Fig. 1(a)]. An  $A_1$  or  $B_1$  beam will then propagate based on

these  $|\phi_A\rangle$ - $|\phi_B\rangle$  states formed in the unit cells along the  $\Gamma$ -K direction. Both of these beams will be characterized by a minimum width that is the height of the unit cell along its long diagonal.

In a metallic structure, where the coupling is of short range, as described by the TB model, the coupling strength between an incident beam and the first resonance modes excited in the structure is decisive for the transmission, since the magnitudes of these resonance modes determine those of the following along the propagation direction, thus the beam transmission. Moreover, for an EM beam with wave vector close to the quasi-triangular iso-frequency contours of the Dirac cones, the above discussion suggests the importance for the incident beam to excite  $|\phi_A\rangle$ - $|\phi_B\rangle$  bonding or anti-bonding states, in the first rhombic unit cells, at the sample edges for an optimum transmission. It is therefore interesting to investigate the EM beam propagation for different local incident conditions at the sample edges. This can be achieved by use of narrow incident beams, of widths of the structure period scales, that will allow to selectively interact with specific local structure configurations, to probe the coupling between the incident field and the local resonance modes associated to the Dirac cones at elementary structure scales.

### III. NARROW ELECTROMAGNETIC BEAM PROPAGATION

#### A. Armchair edge

There are three expected propagation directions for the transmitted beams from the armchair edge, a central beam in the same direction as the incident beam, and two side beams at  $\pm\pi/3$  angles relative to the central one [see Fig. 1(a), (c) and (d)]. The propagation directions are perpendicular to three families of rhombic unit cells, that allow the formation of coupled  $|\phi_A\rangle$ - $|\phi_B\rangle$  pairs mentioned in Sec. II.

The incident beam can only impinge on entire unit cells that are parallel to the edge, rather than on that at  $\pm\pi/3$  angles. At local scale, there are two tile patterns at this edge, an A-B and a B-A tile pair. Here we consider two sample configurations, both  $16 \times 16$  periods in size, characterized by an aspect ratio  $\sqrt{3}$  ensuring the same path lengths for the central and side beams. They offer two armchair edges shifted by a half period in the  $x$  direction, bringing forth respectively an A-B and a B-A tile pair at the edge center [see Fig. 1(a)]. These two cases will be referred to as AB and BA cases hereinafter.

We consider an incident beam of width of the lattice period along  $y$  axis,  $\sqrt{3}a$ , that covers the height of a unit cell along its long diagonal direction. The beam is TM polarized and emitted by a line source of length  $\sqrt{3}a$ , placed close to the sample left edge center. For these two cases, the incident beam impinges respectively on an A-B and a B-A tile pair. The transmissions are considered in

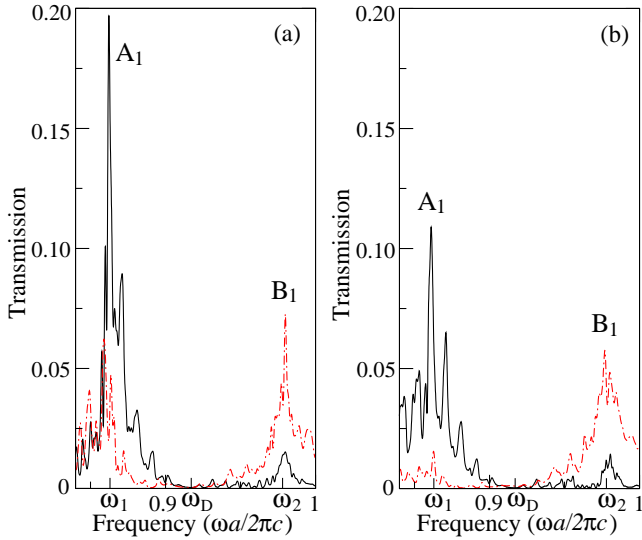


FIG. 2. Transmission spectra for the armchair incidence for the AB [(a)] and BA [(b)] cases in the center (solid lines) and side beam (dash-dotted lines) directions in the vicinity of the Dirac frequency.

two out-going regions. One, with the same width  $\sqrt{3}a$  as the incident beam, is placed at the opposite side of the sample in front of the incident beam for the central beam direction; the other, with width  $2a$ , at the sample upper side (a zigzag edge), at  $\pi/3$  angle relative to the incident direction, for one of the side beams. Here we choose  $2a$  for the side beam direction, since both bonding and anti-bonding states in a unit cell span two periods at the zigzag edge. Using an incident Gaussian beam centered at  $\omega_D$ , the transmission spectra, obtained using the FDTD method and normalized to the incident flux, are displayed in Fig. 2. One can see that maximum transmission peaks are obtained at frequency levels close to  $\omega_1$  and  $\omega_2$ , corresponding respectively to the  $A_1$  and  $B_1$  beams associated to the lower and upper part of the Dirac cones, along the central and the side directions. Their counterparts, i.e., the transmission peaks for the same beams but along the side and central directions, are much weaker. This is comparable to the results of the previous work [19].

Moreover, for the AB case, the central  $A_1$  beam displays a much stronger transmission peak than the side  $B_1$  beam, in spite of the non-negligible transmission for the  $A_1$  beam in the side beam directions. Indeed, the side  $B_1$  beam transmission peak is only about one third of that of the central  $A_1$  beam. The situation is drastically different for the BA case, where the central  $A_1$  beam displays a much weaker transmission peak that is only about half that of the central  $A_1$  beam in the AB case, while the transmission peak of the side  $B_1$  beam, with a difference of only about 20%, is close to its counterpart in the AB case.

The  $A_1$  and  $B_1$  beam propagations at their respective transmission peak frequencies are obtained using the

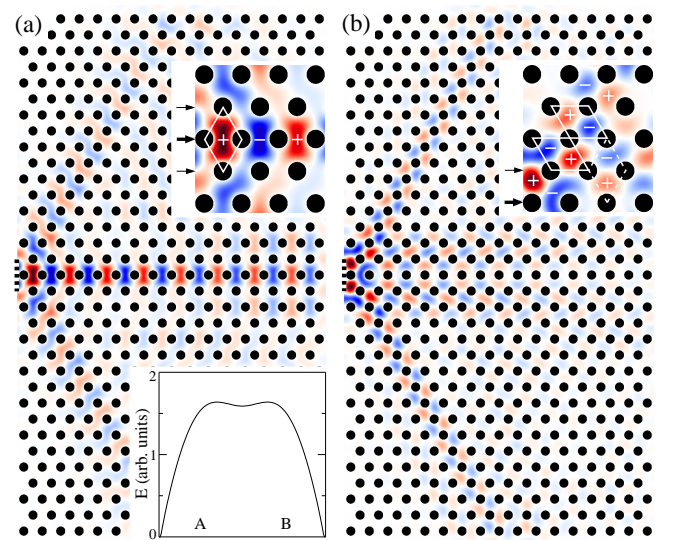


FIG. 3. Electric field distributions of the  $A_1$  [(a)] and  $B_1$  [(b)] beams corresponding to the two maximum transmission peaks in Fig. 2(a) for the AB case, with the thick dashed line at the sample left side indicating the line source position. The upper part insets show a magnified region in the vicinity of the impact zone, with the thick and thin arrows indicating the incident beam axes and edges, and the  $\pm$  signs the field polarities. The unit cells in the central [(a)] and side beam [(b)] directions are delimited by solid lines, and that related to the  $B_1$  beam along the incident beam edge in the central direction by dashed lines [(b)]. The lower part inset in (a) shows the electric field magnitude along the long diagonal of the unit cell, passing by the A and B tiles, in the upper inset.

FDTD method, and images of the electric field distributions are displayed in Figs. 3 and 4. These two figures show that, except in the vicinity of the impact zones for the  $B_1$  beams (this point will be discussed in the following), the electric fields of the  $A_1$  and  $B_1$  beams are formed by resonance modes in the unit cells along their propagation directions, with polarities characterized, respectively, by a mirror and a mirror inversion symmetry with respect to the plane formed by their respective propagation axis and the  $y$  axis, in agreement with the discussion in Sec. II that the beam propagation can be considered as being based on series of bonding or anti-bonding states formed in the unit cells.

Moreover, Figs. 3 and 4 illustrate the relationship between the incident beam and the mode excitation in the two samples. For the AB case, as shown in Fig.3(a), the incident beam can excite an  $A_1$  beam of minimum width, that corresponds to the unit cell height as mentioned in Sec. II, immediately from the impact zone. Indeed, the incident beam impinges on a unit cell formed by an A-B tile pair, and a bonding state is formed in the impacted unit cell through the coupling between the  $|\phi_A\rangle$  and  $|\phi_B\rangle$  modes in the two tiles, as shown in the upper inset of Fig. 3(a). The  $A_1$  beam can be considered as being directly coupled to the incident field.

In the BA case, on the contrary, the incident beam can

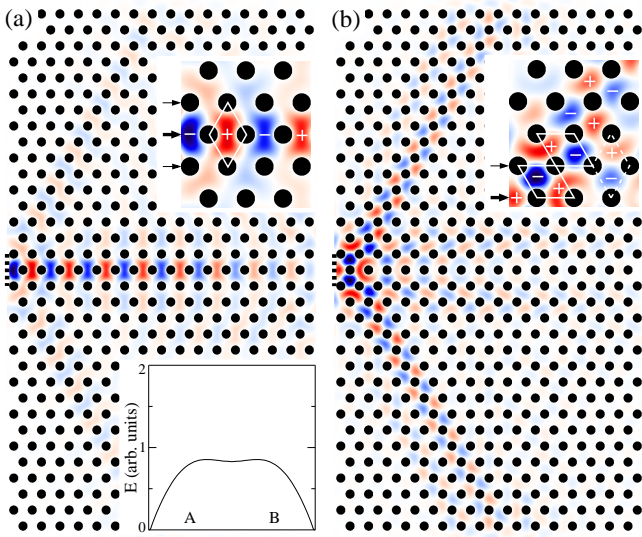


FIG. 4. Same disposition as in Fig.3, but for the BA case and corresponding to the two maximum transmission peaks in Fig. 2(b).

not excite directly the same  $A_1$  beam, like in the AB case, in the immediate impact zone. In fact, here the beam impinges on a B-A tile pair, in which a bonding state between  $|\phi_B\rangle$  and  $|\phi_A\rangle$  modes can not be formed due to the lack of coupling, as discussed in Sec. II. Indeed, as shown in the upper inset of Fig. 4(a), a such state is formed further inside the sample, in the rhombic unit cell situated behind the B-A pair. The coupling between the incident beam and the  $A_1$  beam can be considered as being indirect by comparison with the AB case.

In order to further probe the coupling effect between the incident field and the resonance modes, let us consider the electric field distribution of the  $|\phi_A\rangle$ - $|\phi_B\rangle$  bonding state in the first unit cell in front of the incident beam, at the beginning of the transmitted  $A_1$  beam of respectively the two cases. The field distributions along the long diagonal of the unit cells are displayed in the lower insets of Figs. 3(a) and 4(a). These figures show that, for the same incident beam, the field magnitude in the first unit cell in the AB case is almost twice that in the BA one, confirming that the coupling between the incident field and the  $A_1$  beam is more efficient in the AB case. Moreover, these figures confirm that the field distributions in these two cases display a mirror symmetry with respect to the  $xz$  plane, and can indeed be considered as bonding states formed by a pair of  $|\phi_A\rangle$  and  $|\phi_B\rangle$  modes.

Concerning the side  $B_1$  beams in both cases, their weak transmissions can be related to the local field distributions created by the incident beams. Indeed, due to the  $B_1$  beam propagation directions at  $\pm\pi/3$  angles, the first unit cells at the beginning of the paths are not totally exposed to the incident beam, and that anti-bonding states can not be directly excited by the incident fields in these unit cells. In fact, as shown in Figs. 3(b) and 4(b), the resonances modes are irregularly distributed in the

vicinity of the impact zones, with some of them extending outside the tiles. The local fields in the first unit cells can not be considered as anti-bonding states between  $|\phi_A\rangle$  and  $|\phi_B\rangle$  pairs, and they lack clearly the mirror inversion symmetry with respect to the plane defined by the beam axis and the  $z$  axis (we will show below that this can also be seen in terms of the electric field magnitudes in the unit cells). However, thanks to their polarity distributions, with opposite electric field polarities in the two tiles of the unit cells, these modes can be constructively coupled to the anti-bonding states on the propagation paths. Besides, as we can see in Figs. 2, 3(b) and 4(b), although the  $B_1$  beams is inhibited along the central axis of the incident beams, due to the incompatibility between the mirror symmetry of the latter and the mirror inversion symmetry of the former [19], there is weak transmission in the central direction along the incident beam edges. This can be attributed to mode excitations at the edges of the incident beams [see the insets in Figs. 3(b) and 4(b)], where the latter do not have mirror symmetry. The local fields formed at the sample edges, where the latter intercept the beam edges, display opposite polarities along  $y$  axis, due to the irregularly extended spatial distribution of certain modes, and lead to  $B_1$  beams propagating in the central direction (see the unit cells delimited by dashed lines in the above figures). These points will be further discussed in the following.

## B. Zigzag edge

There two expected propagation directions for the transmitted beams from the zigzag edge, at respectively  $\pm\pi/6$  angles relative to the incident direction and perpendicular to two families of rhombic unit cells [see Fig. 1(a), (c) and (d)]. All the transmitted beams in the two directions, associated to either the upper or the lower Dirac cones, are symmetrically compatible with an incident beam, since two transmitted beams together, either two  $A_1$  or two  $B_1$  ones, are described by a mirror symmetry with respect to the  $yz$  plane. For this orientation, an incident beam can only impinge on the A tiles, rather than on a whole unit cell. It can excite directly neither bonding nor anti-bonding  $|\phi_A\rangle$ - $|\phi_B\rangle$  states.

We consider two sample configurations, both  $32 \times 8$  periods in size, offering two zigzag edges shifted by a half period in the  $y$  direction, bringing forth respectively an A tile and an A-A tile pair at the low edge center [see Fig. 1(a)]. These two cases will be referred to as 1A and 2A cases hereinafter.

An incident beam with width  $a$ , covering one period along  $x$  axis, is considered. The beam is TM polarized and emitted by a line source of length  $a$ , placed close to the sample lower edge center, and impinging respectively on an A tile and two half A tiles. The transmission is considered in an out-going region with width  $2a$  (as mentioned above, both bonding and anti-bonding states in a

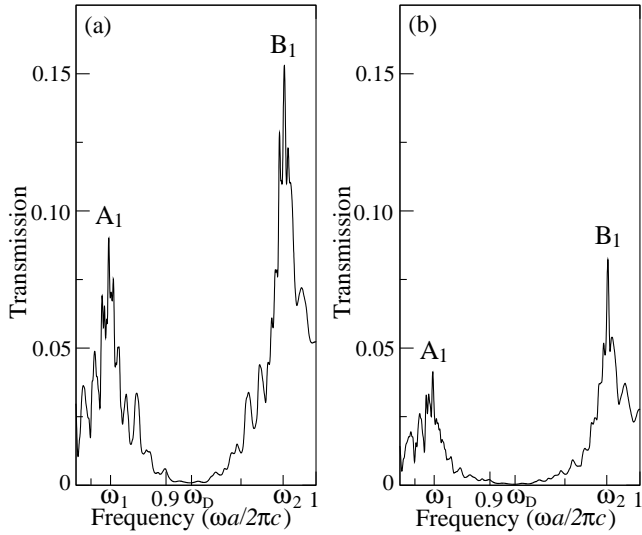


FIG. 5. Transmission spectra for the zigzag incidence for the 1A [(a)] and 2A [(b)] cases in the vicinity of the Dirac frequency.

unit cell span two periods at the zigzag edge) at  $\pi/6$  angle at the sample upper side. For both cases, an incident Gaussian beam centered at  $\omega_D$  is used. The transmission spectra are obtained using the FDTD method and normalized to the incident flux, and displayed in Fig. 5.

Figure 5 shows that, like in the cases of the armchair edges, maximum transmission peaks are obtained at frequency levels close to  $\omega_1$  and  $\omega_2$ , corresponding respectively to the  $A_1$  and  $B_1$  beams associated to the lower and upper part of the Dirac cones. The beam propagation in these samples, for monochromatic waves at the transmissions peak frequencies, is obtained using the FDTD method, and images of the electric field distributions are displayed in Figs. 6 and 7. Like for the armchair incidence, these two figures are in agreement with the discussion in Sec. II, except in the vicinity of the impact zones, that the beam propagation can be considered as being based on series of bonding or anti-bonding states in the unit cells.

Concerning the magnitudes of the beam transmission, Fig. 5 shows that, contrary to the armchair cases, here the  $B_1$  beam transmission peaks display stronger magnitudes than that of the  $A_1$  beams for both the two cases. Indeed, for the 1A case, the maximum transmission peak of the  $B_1$  beam is about 70% higher than that of the  $A_1$  beam, while, for the 2A case, the maximum transmission peak of the  $B_1$  beam is almost twice that of the  $A_1$  one. Moreover, in the latter case, the transmission peaks of both  $A_1$  and  $B_1$  beams are much lower as compared to that in the 1A case, corresponding respectively to about 45% and 55% that of their counterparts.

As pointed out above, neither bonding nor anti-bonding pair states can be excited directly at the zigzag edge, the beam transmissions can be investigated in terms of the coupling effect, that can be probed through

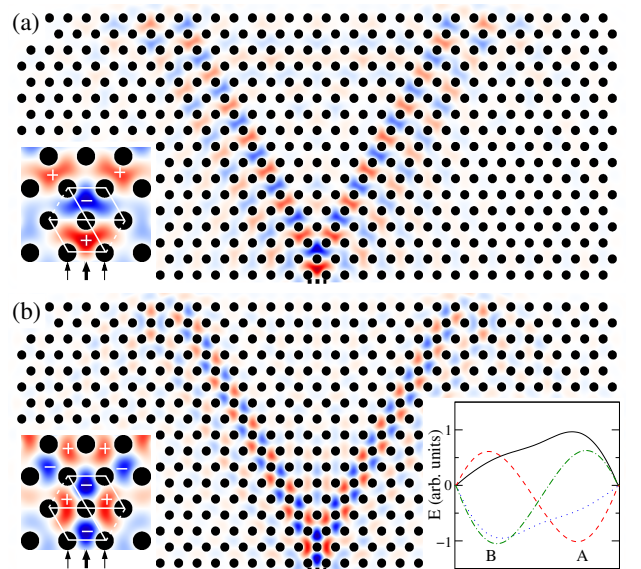


FIG. 6. Electric field distributions of the  $A_1$  [(a)] and  $B_1$  [(b)] beams corresponding to the two maximum transmission peaks in Fig. 5(a) for the 1A case, with the thick dashed line at the sample lower side indicating the line source position. The left part insets show a magnified region in the vicinity of the impact zone, with the thick and thin arrows indicating the incident beam axes and edges, and the  $\pm$  signs the field polarities. The right part inset in (b) shows the electric field magnitudes along the long diagonal, passing by the A and B tiles, of the first and the second unit cells outlined by solid lines in the left insets in respectively (a) (solid and dotted lines) and (b) (dashed and dash-dotted lines).

both the spatial and magnitude distributions of the excited local fields.

Indeed, for both the  $A_1$  and  $B_1$  beams, the local fields in the unit cells at the beginning of the propagation paths (left insets in Figs. 6 and 7) can not be considered as bonding or anti-bonding states between  $|\phi_B\rangle$ - $|\phi_A\rangle$  pairs, though they can be constructively coupled to such states. Moreover, for both beams in the 1A case, the local fields are confined in a hexagon formed by six tiles in the vicinity of the impact zone; while, in the 2A case, the fields are more irregularly distributed, with certain modes extending far out of the tiles.

As far as the field magnitude distributions are concerned, the  $B_1$  beams involve stronger fields than the  $A_1$  beams in both cases. This can be seen on the field magnitude distribution along the long diagonal of the unit cells in the right insets of Figs. 6(b) and 7(b). In the 1A case, the field magnitudes in the B and A tiles of the second unit cell are about 10% and 27% larger for the  $B_1$  beam than for the  $A_1$  one. While, in the 2A case, the magnitudes are about 10% and 32% larger in the A and B tiles of the first unit cell for the  $B_1$  beam than for the  $A_1$  one. This is in agreement with stronger  $B_1$  beam transmission in both two cases.

It is interesting to further compare the coupling be-

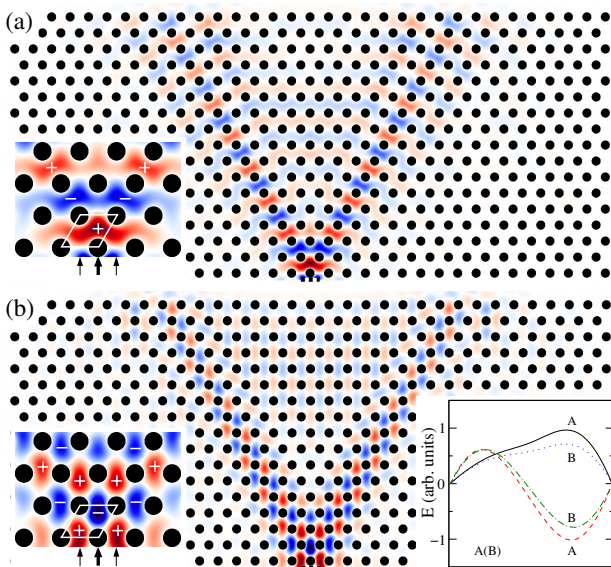


FIG. 7. Same disposition as in Fig.6, except that it concerns the 2A case, with the beams corresponding to the two maximum transmission peaks in Fig. 5(b), and that the right part inset in (b) displays the electric field magnitudes along the long diagonal of the first unit cell outlined by solid lines in the left insets in respectively (a) (dotted line) and (b) (dash-dotted line), together with that in the first unit cell of the 1A case in Fig. 6(a) (solid line) and (b) (dashed line).

tween the incident fields and the local modes in the first unit cells, for respectively the  $A_1$  and  $B_1$  beams, between the 1A and 2A cases. In fact, as shown in the right inset of Fig. 7(b), for the  $A_1$  beams, the field magnitudes along the cell long diagonal in the left and right tiles are about 13% and 35% stronger in the 1A case as compared to the 2A one; while, for the  $B_1$  beams, the field magnitudes are almost the same in the left tiles for the two cases, and that in the right tile in the 1A case is about 29% stronger than that in the 2A case. This shows clearly a stronger coupling for both  $A_1$  and  $B_1$  beams in the 1A case, leading to stronger transmissions.

The right inset of Fig. 7(b) shows also that, for both cases, the excited modes in the first unit cells have stronger magnitude in the central tiles of the incident edges (the left tile of the unit cell), and it is basically in these tiles that the stronger coupling with the incident field is manifested for the two beams of the 1A case.

This can be related to the nature of the excited local fields. As a matter of fact, in the 1A case, the field distributions in the hexagon for the  $A_1$  and  $B_1$  beams can be considered as corresponding respectively to a bonding and an anti-bonding state on the hexagonal ring, similar to that of the  $\pi$  molecular orbitals of Benzene. A description of this classic case can be found in Ref. [24], where the two states are labeled as  $\phi_{2,real}$  and  $\phi_{4,real}$ . Indeed, these field distributions have a mirror symmetry with respect the  $yz$  plane, and, as shown in the right inset in Fig. 6(b), for each beam, the modes in the two tiles

on the incident beam axis have almost the same magnitudes, that are roughly twice stronger than that in the other four tiles (with a factor of about 1.9 and 1.7 for the  $A_1$  and  $B_1$  beams). The formation of these states is not surprising since their frequency levels, resulting from the coupling between neighbor modes on the hexagonal ring, correspond respectively to that of the bonding and anti-bonding states between a neighbor pair. They can thus be excited by incident fields with frequency levels close to  $\omega_1$  and  $\omega_2$ . The incident beam impinges on one of the tiles (the A tile) supporting a mode of large magnitude, developing thus a strong coupling with these states. While, for the two beams in the 2A case, such states can not be excited since the incident beam axis passes between two A tiles. Besides, the incident beams impinge on two half A tiles, the coupling is thus weaker for each mode in an A tile. Moreover, the modes in the central B tile are only indirectly coupled to the incident fields, through the coupling with the two adjacent A tiles, hence their weaker magnitudes as compared to that in the 1A case.

#### IV. DISCUSSION

The above results underline the importance of the coupling between the incident field and the resonance modes at local scales in the beam transmission, associated to the Dirac cones following different K-valleys. Indeed, due to the metallic nature of the structure, as well as the frequency band structure in the vicinity of the quasi-triangular Dirac cone contours, a good transmission necessitates, for an incident field, strong coupling with the local resonance modes, as well as the excitation of resonance mode distributions corresponding to bonding or anti-bonding states in the first unit cells. These aspects are determined by the unit cell exposition and orientation with respect to the incident beam. This point can further be probed by local structure modification that alters the coupling with the incident beam.

Let us consider the AB case, where the side  $B_1$  beam transmission is much weaker than that of the central  $A_1$  beam. As mentioned in Sec III A, anti-bonding states can not be directly excited by the incident beam in the unit cells at the beginning of the  $B_1$  beam paths. The resonance modes are irregularly distributed in the vicinity of the impact zone. And, moreover, the mode excitation at the beam edges lead to transmission in the central direction. However, by creating a structure vacancy by removing the cylinder at the armchair edge center, i.e., on the incident beam axis, we get the transmission spectra in Fig. 8(a) for the same incidence. The transmission peaks for the  $A_1$  and  $B_1$  beams now have similar magnitudes. Indeed, comparing to the original AB case, the  $A_1$  beam transmission peak is decreased by about one third, while the  $B_1$  beam transmission peak increased by about 80%.

This can be related to the change in the coupling con-

ditions at the incident edge. As a matter of fact, the decrease of the  $A_1$  beam transmission can straightforwardly be attributed to the fact that the incident beam can no more be directly coupled to a bonding state, since it now impinges on a B-A tile pair, like in the BA case. The transmission is stronger (by about 25%) compared to the  $A_1$  beam in the latter case, because the incident beam has a larger aperture, the two cylinders at the extremity of the line source being at  $a/2$  away.

Let us focus on the  $B_1$  beam transmission. The electric field of the beam propagation is displayed in Fig. 8(b). As a matter of fact, the  $B_1$  beam transmission peak increase can be attributed to the improved coupling condition for the incident beam, leading to field distribution close to anti-bonding states in the vicinity of the impact zone. Indeed, the removal of the central cylinder leaves exposed locally two portions of armchair edges at  $\pm\pi/3$  angles, allowing a better exposition of the first unit cells, at the beginning of the beam propagation paths, to the incident beam, without the latter being scattered by the central cylinder, ensuring thus a better coupling between the incident field and the resonance modes in these unit cells. This can be seen in the upper inset of Fig. 8(b), that shows that the resonance modes in the vicinity of the impact zone display more regular spatial distributions as compared to the original AB case, and, moreover, they are now all confined inside the triangular tiles of the unit cells along the propagation path. As far as the field magnitudes are concerned, the magnitude distribution [lower inset of Fig. 8(b)] along the long diagonal of the first unit cell at the beginning of the beam path shows that, as compared to the original AB case, where the mode magnitudes display strong difference, with that in the B tile about 21% weaker than that in the A tile, the mode in the B tile in the modified case has its magnitude increased, along with the confinement of its spatial distribution. The two modes in the first unit cell have now closer magnitudes, with that in the B tile only about 7% weaker than that in the A tile (the latter remains almost the same as its counterpart in the original AB case), approaching the field distribution of a  $|\phi_B\rangle-|\phi_A\rangle$  anti-bonding state.

One the other hand, the field distributions at the sample edge, where the latter intercepts the incident beam edges, have no more opposite polarities along  $y$  axis. Indeed, in the original AB case, as shown in the upper inset of Fig. 3(b), the bipolar field distribution at the sample edge is formed due to the irregular spatial distribution of the mode in the B tile in the first unit cell at the beginning of the beam path, that extends to the zone above the beam edge axis (the thin arrow) at the sample edge. In the modified case, on the contrary, all the modes are well confined inside the triangular tiles, and, as shown in the upper inset of Fig. 8(b), the field is vanishingly weak in the same zone. This disfavors the mode excitations at the incident beam edges that lead to beam propagation in the central direction mentioned in Sec. III A. Indeed, as shown by the transmission and the field distribution in

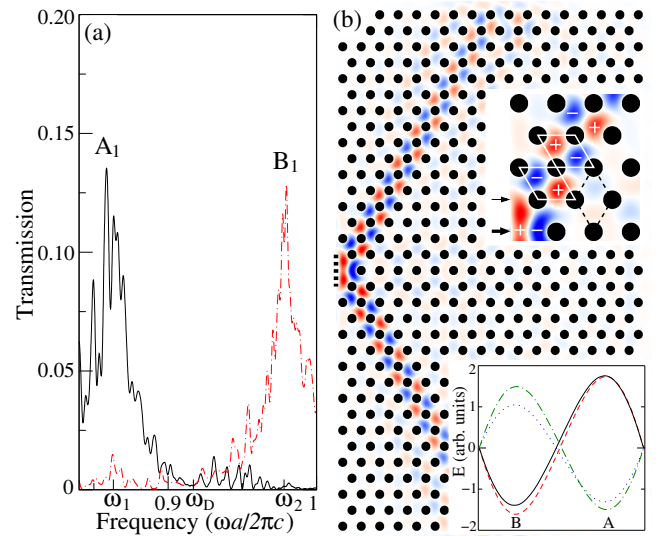


FIG. 8. Transmission spectra for the modified AB case in the center (solid lines) and side beam (dash-dotted lines) directions in the vicinity of the Dirac frequency [(a)]. And the electric field distribution of the  $B_1$  beam corresponding to the maximum transmission peak in the side beam direction [(b)], with the thick dashed line at the sample left side indicating the line source position. The upper part inset in (b) shows a magnified region in the vicinity of the impact zone, with the thick and thin arrows indicating the incident beam axis and edge, and the  $\pm$  signs the field polarities. The unit cells in the side beam direction are delimited by solid lines, and that related to the  $B_1$  beam along the incident beam edge in the central direction by dashed lines. The lower part inset shows the electric field magnitude along the long diagonal, passing by the A and B tiles, of the first (dashed line) and second (dash-dotted line) unit cells along the propagation direction outlined in the upper inset, together with that in the first (solid line) and second (dotted line) unit cells of the original AB case in Fig. 3(b).

Fig. 8, the  $B_1$  beam transmission in the central direction is almost absent. This can further be confirmed by the field magnitude distributions [lower inset in Fig. 8(b)] in the second unit cell from the beginning of the path [upper insets in Figs. 3(b) and 8(b)]. The field magnitudes are stronger for both modes in the B and A tiles in the modified case, with respectively an increase of about 42% and 14% as compared to the original case. This can be attributed to the quasi-absence of the transmission in the central direction. Moreover, with a magnitude difference of only about 0.3% between the modes in the B and A tiles, the field in this unit cell is almost that of a pure  $|\phi_B\rangle-|\phi_A\rangle$  anti-bonding state. This example confirms that the transmission of a narrow incident beam is favored by the excitation of resonance modes the closest to bonding or anti-bonding states in the first unit cells, as well as a strong coupling with these modes.

It is worth pointing out that the results concerning the armchair edge in the present investigation are comparable to that in the previous work [19]. The quantitative

differences in the transmission values can be attributed to two factors. On one hand, the previous work involves a much larger incident beam width, and the transmission should thus be considered as resulting from a hybrid of the AB and BA cases of the present work. On the other hand, the metallic waveguide used in the previous work prevents the incident beam spreading and thus reinforces its transmission in the sample.

The present investigation allows us to understand the interaction between an incident EM beam and the resonance states, associated to both the lower and upper parts of the Dirac cones for different valleys, at elementary structure scales reaching the size of these resonance states. It provides information on the relationship between the structure configurations and the transmission of an incident EM beam, with wave vector close to the quasi-triangular iso-frequency contours of the Dirac cones, at both the armchair and zigzag edges, and may find application in valley photonics for tuning and optimizing the beam transmission in the design of various beam collimation and splitting devices to convey information and address different valleys. Moreover, since this investigation deals with EM beam width at its minimum limit for a metallic structure, its results can be of specific interest to miniaturized low-power photonic systems.

## V. CONCLUSION

This investigation highlights the importance of the coupling effect between an incident EM beam, with wave vector close to the quasi-triangular iso-frequency contours of the Dirac cones, and the local resonance modes at both the armchair and zigzag edges of the graphene-like triangular metallic structure for the beam transmission. Indeed, by probing the coupling effect at elementary structure scales with narrow incident EM beams, it shows strong excitation difference in the first unit cells, following their positions and orientations with respect to the incident fields. This in turn determines the beam transmission associated to the upper and lower parts of the Dirac cones for different K-valleys. Large transmission is obtained for incident conditions allowing strong coupling between the incident fields and the resonance modes in the first unit cells at the incident edges, and leading to field distributions corresponding or close to bonding or anti-bonding states for these modes. This work allows understanding the particularity of the graphene-like metallic photonic structure in its interaction with the EM waves at scales down to the size of local resonance states. It may find application in valley photonics in the designs of beam collimation and splitting devices for information processing, by providing information for tuning and optimizing the beam transmission in various conditions, and, in addition, be of specific interest to miniaturized photonic systems.

- 
- [1] O. Peleg, G. Bartal, B. Freedman, O. Manela, M. Segev, and D. N. Christodoulides, *Phys. Rev. Lett.* **98**, 103901 (2007)
  - [2] R. A. Sepkhanov, Ya. B. Bazaliy, and C. W. J. Beenakker, *Phys. Rev. A* **75**, 063813 (2007)
  - [3] S. Raghu and F. D. M. Haldane, *Phys. Rev. A* **78**, 033834 (2008)
  - [4] X. Huang, Y. Lai, Z. H. Hang, H. Zheng, and C. T. Chan, *Nature Mater.* **10**, 582 (2011)
  - [5] J. L. Garcia-Pomar, A. Cortijo, and M. Nieto-Vesperinas, *Phys. Rev. Lett.* **100**, 236801 (2008)
  - [6] A. Rycerz, J. Tworzydło, and C. W. J. Beenakker, *Nature Physics* **3**, 172 (2007)
  - [7] J.-W. Dong, X.-D. Chen, H. Zhu, Y. Wang, and X. Zhang, *Nature Materials*, **16**, 298 (2017)
  - [8] T. Ma and G. Shvets, *New J. Phys.* **18**, 025012 (2016)
  - [9] J.-W. Dong, X.-D. Chen, H. Zhu, Y. Wang, and X. Zhang, *Nat. Mater.* **16**, 298 (2016)
  - [10] M. Plihal and A. A. Maradudin, *Phys. Rev. B* **44**, 8565 (1991)
  - [11] S. Bittner, B. Dietz, M. Miski-Oglu, P. Oria Iriarte, A. Richter, and F. Schäfer, *Phys. Rev. B* **82** 014301 (2010)
  - [12] K. Wang, *Mater. Res. Express*, **3**, 115007 (2016)
  - [13] K. Wang, *Phys. Rev. B* **97**, 125146 (2018)
  - [14] F. D. M. Haldane and S. Raghu, *Phys. Rev. Lett.* **100**, 013904 (2008)
  - [15] K. Wang, *J. Opt. Soc. Am. B* **31**, 1273 (2014)
  - [16] R. Saito, G. Dresselhaus, and M. S. Dresselhaus, *Phys. Rev. B* **61**, 2981 (2000)
  - [17] F. Deng, Y. Sun, X. Wang, R. Xue, Y. Li, H. Jiang, Y. Shi, K. Chang, and H. Chen, *Opt. Express*, **22**, 23607 (2014)
  - [18] Z. Wang and F. Liu, *ACS Nano*, **4**, 2459 (2010)
  - [19] K. Wang, *Phys. Rev. B* **100**, 115140 (2019)
  - [20] C. Park, *J. of Appl. Phys.* **118**, 244301 (2015)
  - [21] M. M. Sigalas, C. T. Chan, K. M. Ho, and C. M. Soukoulis, *Phys. Rev. B* **52**, 11744 (1995)
  - [22] See, for example, N. W. Ashcroft, N. D. Mermin, *Solid State Physics* (Saunders College, Philadelphia 1976), Chap. 10
  - [23] See, for example, J. R. Ferraro, and K. Nakamoto, *Introductory Raman Spectroscopy* (Academic Press, 1994), p.310 & p.337
  - [24] I. N. Levine, *Quantum Chemistry*, 7th Ed. (Pearson, Upper Saddle River, NJ 2014), pp.606-609